INCLUSIVE PUBLISHING
TRUSTED SCIENCE

PAPER • OPEN ACCESS

Monitoring self-discharge in a dual-ion battery using *in situ* Raman spectro-electrochemistry

View the article online for updates and enhancements.

Materials Research Express

PAPER

Monitoring self-discharge in a dual-ion battery using *in situ* Raman spectro-electrochemistry

Ismail Yussuf Hassan, Wessel W A van Ekeren, Antonia Kotronia, Maria Hahlin and Habtom D Asfaw

Department of Chemistry-Ångström laboratory, Uppsala University, Lägerhyddsvägen 1, 75121 Uppsala, Sweden

E-mail: habtom.desta.asfaw@kemi.uu.se

Abstract

A dual-ion battery employs two graphite electrodes to host cations and anions from the electrolyte. The high potential required to intercalate anions in graphite fully, typically > 5 V versus Li^+/Li, triggers electrolyte decomposition and dissolution of the aluminium current collector. Such unwanted reactions significantly aggravate self-discharge, leading to low energy efficiency and shorter cycle life. This study investigates changes in graphite structure during the intercalation of bis(fluorosulfonyl) imide (FSI) anion in 4 M LiFSI in ethyl methyl carbonate (EMC) and evaluates the stability of the associated FSI-intercalated graphite compounds using *in situ* Raman spectroscopy. The results highlight the critical importance of the duration the GICs remain in contact with the electrolyte, before the acquisition of the Raman spectra. Accordingly, the GICs with high FSI anion content exhibited only short-term stability and lost anions during open-circuit potential relaxation; only dilute GIC phases (stages $\geqslant$ IV) were sufficiently stable in the presence of the concentrated electrolyte. Furthermore, the formation of gaseous products during the charge–discharge cycles was verified using a 3-electrode cell with a pressure sensor. Future studies can adopt the experimental strategy developed in this work to assess the efficacy of electrolyte additives in mitigating self-discharge in DIBs.

1. Introduction

Owing to its layered structure, interlayer spacing of 3.35 Å, and electronic structure, graphite can host both anions and cations, forming donor- and acceptor-type graphite intercalation compounds (GICs) [1–4]. Some acceptor-type GICs have found applications as positive electrodes in dual-ion batteries (DIBs), an emerging technology promising for stationary energy storage applications [5–15].

Most anion intercalation in graphite occurs in the 4.3 to 5.2 V versus Li^+/Li range, which raises a serious challenge associated with the degradation of state-of-the-art electrolytes, Al current collector, and binders [7, 16, 17]. These oxidative reactions have been cited as possible reasons for coulombic efficiencies of $< 100\%$ and quick self-discharge in DIBs using anion-intercalated GICs [17]. Thus, there is a pressing need for electrolytes with high oxidative stability and the ability to form protective layers at the electrode–electrolyte interfaces [7, 16–19]. So far, the reversible graphite-graphite DIB chemistry has been enabled by electrolytes composed of fluorinated salts, solvents and additives, which can withstand electrochemical reactions above 5 V versus Li^+/Li [20–23] The most common electrolytes employed in DIBs are concentrated-salt organic carbonates and ionic liquids (IL) [20, 24–26]. A wide variety of salts, including those containing PF_6^-, BF_4^-, ClO_4^-, bis(fluorosulfonyl)imide (FSI) and bis(trifluoromethane sulfonyl)imide (TFSI) anions have extensively been studied in electrolytes for DIBs [15, 16, 22, 27, 28]. Though salts containing PF_6^- and BF_4^- are efficient in passivating Al current collectors, they have relatively limited solubility or pose safety concerns linked to HF generation, particularly in the case of PF_6^- [29]. As a result, salts containing FSI and TFSI anions are preferable from a safety and performance perspective. Along with carboxylate esters and linear carbonate solvents, these salts allow to prepare electrolytes with concentrations of up to 5 M, achieving an optimum trade-off between

ionic conductivity and energy density [9, 16, 30]. However, concentrated electrolytes of TFSI and FSI-based salts still suffer from long-term degradation and Al dissolution, causing poor coulombic efficiency (CE) and limited cycle life of DIBs [7, 16]. Some fluorinated electrolyte additives such as $LiPF_6$, $LiBF_4$, lithium difluoro(oxalate) borate (LiDFOB) and methyl difluoroacetate have been shown to some extent to mitigate parasitic reactions [22, 31]. In the absence of additives that can passivate the electrode–electrolyte interfaces, low coulombic efficiency, short cycle life and aggravated self-discharge were observed [22, 31]. Tools such as XPS and electron microscopy have been used to characterise the insoluble products forming on the surface of graphite electrodes [7, 16]. Full analysis requires characterisation of the species dissolved [32–34] in the electrolyte and the gases evolved [35–39].

The impact of side reactions on long-term charge retention and stability of GICs can be evaluated using various techniques, including x-ray diffraction, Raman spectroscopy, electrochemical dilatometry, online electrochemical mass spectrometry, and x-ray spectroscopy [9, 16, 27, 37, 40–44]. In particular, *in situ* Raman spectroscopy can readily be applied to track structural changes in GICs during anion intercalation and extraction processes [1, 42]. This study applies *in situ* Raman spectroscopy to explore the stability of FSI-intercalated GICs prepared electrochemically in Li-graphite DIBs. Similar to previous studies on other anions, it is proven that FSI intercalation in graphite gives rise to a series of staged GIC phases forming at different potentials. The stability of the FSI-intercalated graphite compounds was explored with the help of Raman spectroscopy and operando gas pressure measurements. Electrochemical tests were performed to determine the optimum potential range required for reversible anion intercalation, assess rate capability, and track changes in the structure of the GIC phases occurring during self-discharge in a 4 M LiFSI-EMC electrolyte. The FSI-intercalated GIC electrodes were stored at open circuit potentials in the electrolyte to investigate their oxidative stability. Any structural changes were monitored using *in situ* and *ex situ* Raman scattering measurements. The total gas pressure was measured *operando* in a three-electrode cell consisting of a $Li_4Ti_5O_{12}$ (LTO) negative electrode, a positive graphite electrode, and a lithium reference embedded within the separator.

2. Method

2.1. Electrode and electrolyte preparation

The graphite electrodes contained 95 weight % KS6 graphite (KS6 TIMREX® from IMERYS, up to 20 μm in size, ~26 $m^2\,g^{-1}$ BET specific surface area) and 5 wt% carboxymethyl cellulose (CMC, Leclanche®). A slurry was prepared by mixing the active material and binder in de-ionised water and homogenised for about 30 min at 20 Hz using a Retsch PM400 shaker. The slurry was then cast onto carbon-coated Al foil using a doctor blade (ZFR 2040, Zehntner® testing instruments) on a bar-coater (RK® Control Coater). The coating was allowed to dry at ambient conditions. Similarly, $Li_4Ti_5O_{12}$ (LTO) electrodes were prepared from a slurry containing LTO (HOMBITEC, Venator), SuperP carbon (Alfa Aesar®), and CMC in 85:10:5 weight proportion and blended at 30 Hz. Then, 13- and 20-mm diameter disk electrodes were punched out from the coating using a perforator (Hohsen® electrode puncher) and dried under vacuum (Büchi Glass Oven B-585) at 120 °C over 12 h in an Ar-filled glovebox (GS Glovebox Systemtechnik, $O_2 < 1$ ppm, $H_2O < 1$ ppm). On average, the areal mass loadings of graphite and LTO electrodes were about 4 and 3.3 $mg\,cm^{-2}$, respectively.

To prepare a 4 M LiFSI electrolyte, the desired amount of lithium bis(fluorosulfonyl)imide (LiFSI, 99.9%, Solvionic) was dissolved in ethyl methyl carbonate (EMC, Sigma-Aldrich®) to make up a 4 M concentration. The LiFSI salt was dried at 60 °C for 36 h while EMC was dried over activated molecular sieves (3 Å) for at least 48 h and filtered through a 200 nm PTFE membrane before use. The electrolyte mixture was stirred overnight for at least 12 h before use. Using a Karl Fischer coulometer (Metrohm®), the water content in the electrolyte was determined to be < 7 ppm.

2.2. Electrochemical testing

Pouch cells were assembled in two- and three-electrode configurations using positive graphite electrodes, lithium (16 mm) or LTO (13–18 mm) as the negative electrodes and lithium reference electrodes. Glass fibre membrane (Whatman®, 240 μm, 20 mm in diameter) and Celgard® 2325 (25 μm in thickness, 9 cm^2 area, 39% porosity), which were soaked in 100–150 μl of the 4 M LiFSI in EMC electrolyte, were used as the separators. Cyclic voltammetry experiments were conducted on MPG2 potentiostats (from BioLogic®) at a scan rate of 0.1 $mV\,s^{-1}$ with four different potential cut-offs, 5.0, 5.1, 5.2, and 5.3 V versus Li^+/Li, to assess the optimum working potential ranges. Furthermore, galvanostatic measurements were conducted at 20 $mA\,g^{-1}$ between 3 and 5 V versus Li^+/Li using Arbin BTS and MPG2 (BioLogic®) cyclers. In addition, rate tests were performed at 20, 50, 100, 200, and 500 $mA\,g^{-1}$ on 3-electrode DIB.
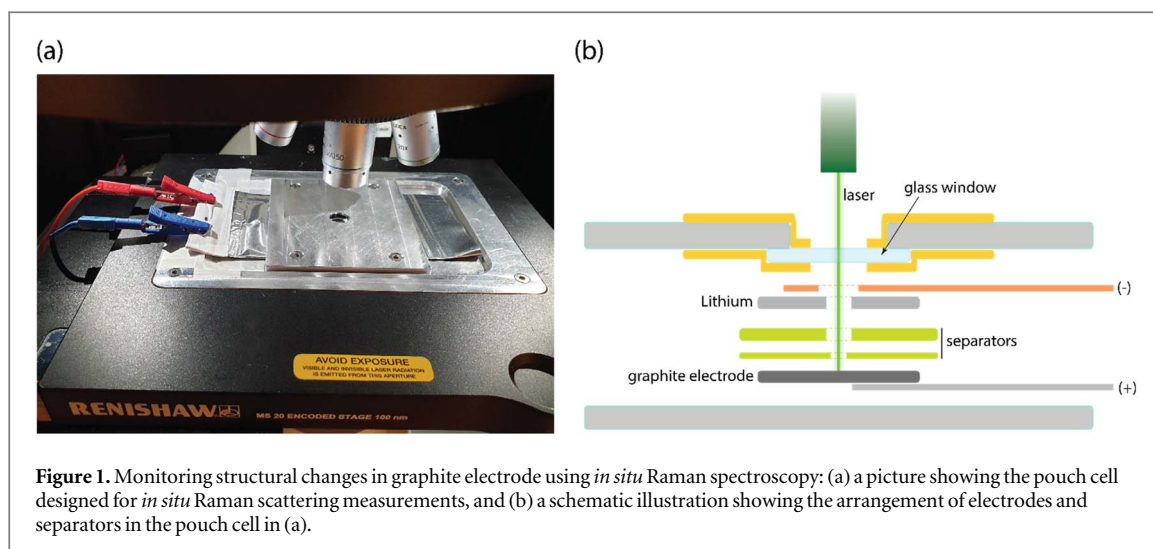
Figure 1. Monitoring structural changes in graphite electrode using *in situ* Raman spectroscopy: (a) a picture showing the pouch cell designed for *in situ* Raman scattering measurements, and (b) a schematic illustration showing the arrangement of electrodes and separators in the pouch cell in (a).

2.3. Raman spectroscopy

Renishaw® inVia Ramanscope, equipped with a 50-mW 532 nm laser, was employed to collect the Raman spectra of pristine and cycled graphite electrodes. During measurements, the laser was focused on selected sample spots using a 50x objective lens. The laser power was fixed at 1% with a 20-s exposure time to prevent sample and electrolyte damage due to overheating. Before the measurements, the instrument was calibrated to set the peak for the Si wafer at 520.5 cm^{-1}. The spectra were measured on several spots on each sample, and their cumulative intensity was used to provide the most representative spectrum. The background, due to fluorescence, was fitted to a polynomial function and stripped from some of the spectra.

In situ measurements were conducted on a pouch cell fitted with a borosilicate glass window through which the laser signal impinged on the graphite electrodes (see figures 1(a) and (b)). The Raman spectra were collected at different states of charge and discharge. The cells were subjected to galvanostatic charge and discharge at 20 mA g^{-1} to various potentials: 4.5, 4.7, 4.85, and 5.0 V during charging, and 4.6, 4.4, 4.2, 4.0 and 3.0 V during discharging. The Raman spectra were acquired *in situ* directly after the current interruption, limiting the extent of self-discharge. For ex situ Raman scattering, more than 15 cells were charged and discharged at 20 mA g^{-1} to different potential cut-offs (4.5, 4.7, 4.85, and 5.0 V versus Li$^+$/Li on charge, 4.6, 4.2, 4 and 3.0 V versus Li$^+$/Li on discharge), and allowed to rest at open circuit potential (OCP) and ambient conditions for 1 to 168 h (1 week). The selected potentials represented the transitions between various FSI anion intercalation/deintercalation stages in graphite. The graphite electrodes were removed from the cells inside a glovebox for subsequent Raman spectroscopy analysis.

Finally, self-discharge tests were performed on an MPG Biologic potentiostat at 20 mA g^{-1} in the 3–5.0 V voltage range. The cells were charged to 5.0 V and left to relax at OCP for about 100 h, after which the graphite electrodes were recovered for further Raman spectroscopy measurements. Non-linear curve fitting was carried out in Rampy [45] using Breit-Wigner-Fano (BWF) [46] and Pseudo-Voigt functions.
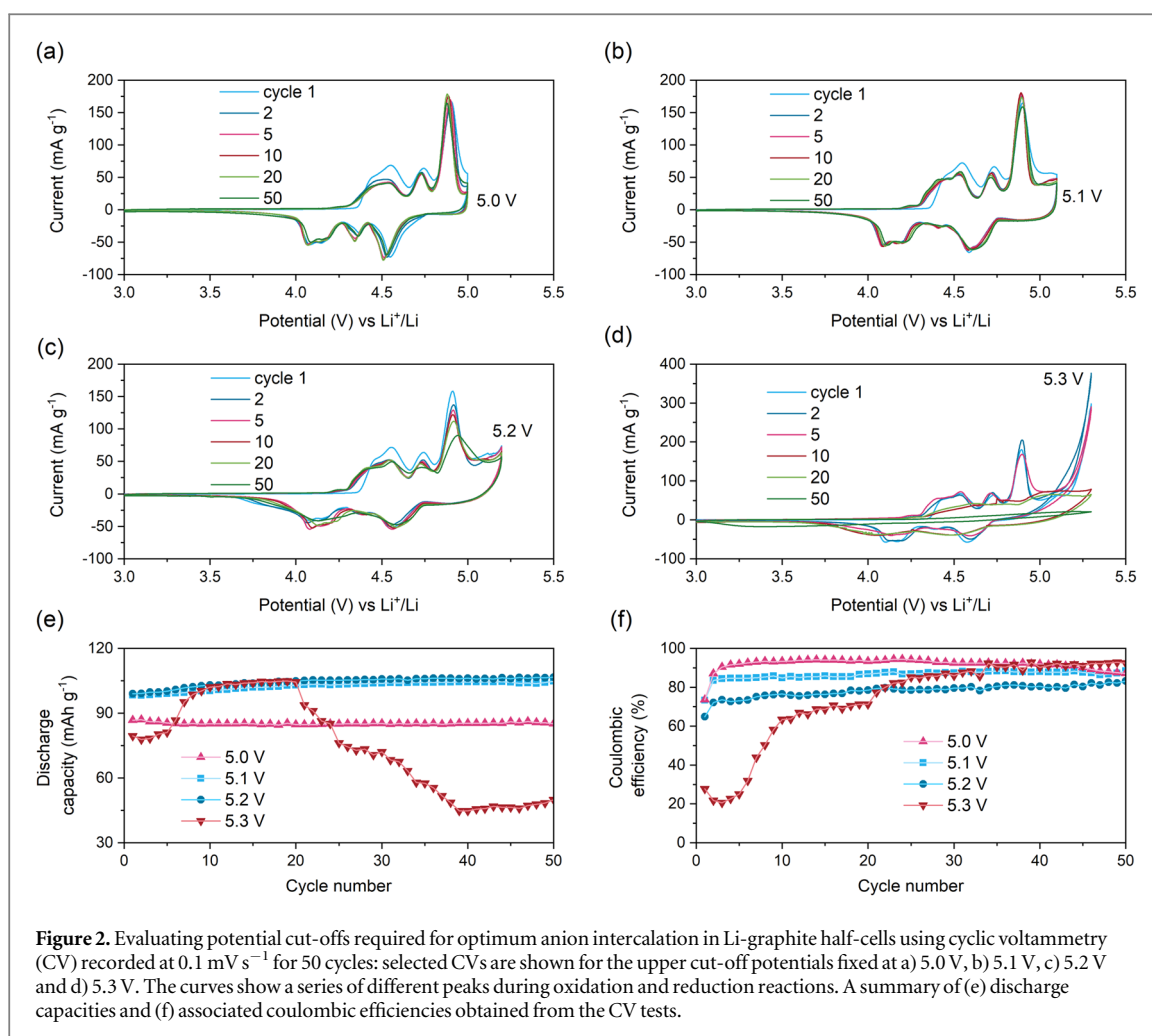
2.4. Operando gas pressure monitoring

The pressure developed due to gaseous decomposition products during anion intercalation and de-intercalation was monitored using the PAT-cell from EL-CELL®. Within this setup, a maximum leakage rate of 0.3 mbar h^{-1} was guaranteed by helium leak tests. The three-electrode setup consisted of a Li$_4$Ti$_5$O$_{12}$ (LTO) counter electrode, a graphite working electrode, and a Li metal ring as the reference electrode. LTO electrodes were used instead of lithium metal to minimise the reductive degradation of the electrolyte and its contribution to the total gas pressure. The galvanostatic tests were conducted on the cells kept in a climate chamber at 30 °C.

3. Results and discussion

3.1. Electrochemical performance

Figures 2(a)–(d) shows a selection of the cyclic voltammograms (CVs) with different upper potential cut-offs. The CVs exhibit multiple oxidation and reduction peaks, which characterise the electrochemical intercalation of anions in graphite resulting in the formation of different phases of acceptor-type GICs [16]. Most FSI intercalation occurred at potentials above 4.3 V, whereas most deintercalation started at <4.7 V. The characteristic signatures of staging intercalation reactions in graphite were visible regardless of the cut-off

Figure 2. Evaluating potential cut-offs required for optimum anion intercalation in Li-graphite half-cells using cyclic voltammetry (CV) recorded at 0.1 mV s^{-1} for 50 cycles: selected CVs are shown for the upper cut-off potentials fixed at a) 5.0 V, b) 5.1 V, c) 5.2 V and d) 5.3 V. The curves show a series of different peaks during oxidation and reduction reactions. A summary of (e) discharge capacities and (f) associated coulombic efficiencies obtained from the CV tests.

potential. However, the peaks disappeared along with a sharp decline in capacity over 20 cycles when the cut-off was extended to 5.3 V versus Li$^+$/Li. The trends in the discharge capacities and associated coulombic efficiencies for the 50 cycles (figures 2(e) and (f)) reveal clear dependence on the cut-off potentials. As the potential increased from 5.0 V to 5.1 and 5.2 V, the discharge capacities increased from 80 to 105 mAh g^{-1}, even though the coulombic efficiency deteriorated [16]. This observation confirms that complete anion intercalation may require > 5 V in order to form stage-I GIC in which all the interlayer spaces are occupied [27, 47]. Extending the cut-off potential to 5.3 V undermined electrochemical performance (figures 2(d)–(f)), manifesting in very low coulombic efficiency (30% versus 72% at 5.0 V for the initial cycle) and quick capacity fading. Decreasing CE was observed in the order 5.0 > 5.1 > 5.2 > 5.3 V versus Li$^+$/Li. Therefore, the potential cut-off was eventually fixed at 5.0 V for further tests conducted in this study. Tests were conducted on Li-Al cells to evaluate the stability of the Al current collectors in the same electrolyte in the potential range of 3 to 5.2 V. A maximum current of 2.08 mA cm^{-2} was observed in the first cycle CV (see figure S1), which diminished to 1.59 and 0.64 mAcm^{-2} at the 2nd and 20th cycles, respectively. The reason behind this observation can be attributed to depletion of free solvent molecules in the concentrated electrolyte, and inhibition of the anodic Al dissolution as the electrolyte got saturated with [Al(FSI)$_x$]$^{3-x}$ complexes after the first few cycles [16].

DIBs are expected to perform reasonably well at high rates since they use cations and anions in the electrolytes, for which a high Li$^+$ transport number is unnecessary. The galvanostatic data in figure S2 (a) and (c) given for currents of 50–1000 mA g^{-1} showed that the capacity decreased slightly to ∼57 mAh g^{-1} at 2 A g^{-1} amounting to approximately 60% capacity retention vis-à-vis the capacity at 50 mA g^{-1} which was ∼ 90 mAh g^{-1}. It should be noted, however, that the coulombic efficiency remained reasonably low for 50 mA g^{-1} 88%–97% and increased to 99% as the applied current increased to 2 A g^{-1}. The trend demonstrated that the FSI-intercalated GIC electrodes possessed only short-term stability in the concentrated electrolyte. No long-term prevention of parasitic reactions was achieved. The conclusion was further verified in the self-discharge experiments coupled with Raman scattering and operando gas pressure monitoring discussed in the following sections.
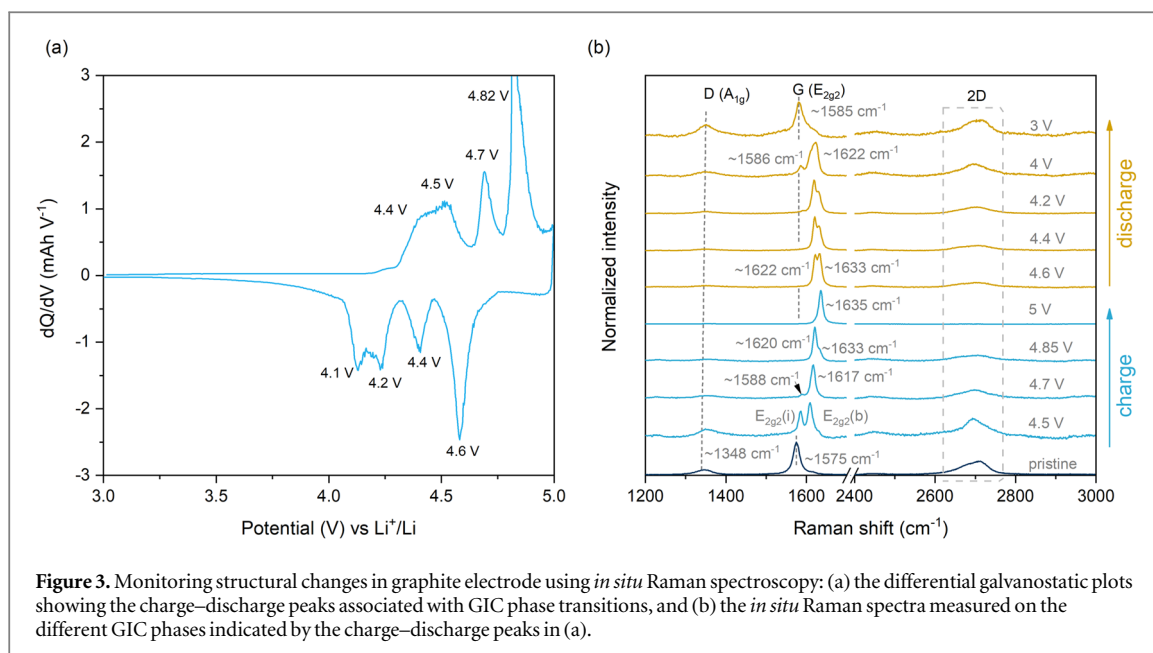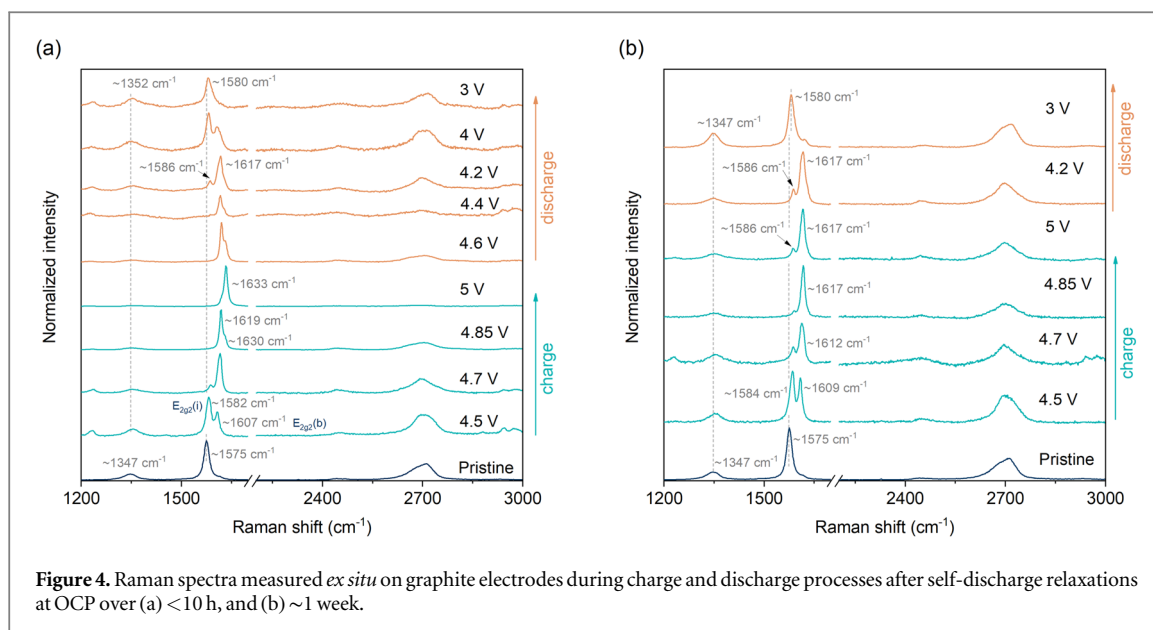
Figure 3. Monitoring structural changes in graphite electrode using *in situ* Raman spectroscopy: (a) the differential galvanostatic plots showing the charge–discharge peaks associated with GIC phase transitions, and (b) the *in situ* Raman spectra measured on the different GIC phases indicated by the charge–discharge peaks in (a).

3.2. Assessing the stability of FSI-intercalated GICs using Raman spectroscopy

The differential capacity vs voltage plot shown in figure 3(a) was used to determine the potentials for the formation and transitions of the staged GICs. Most importantly, four peaks were observed at approximately 4.4, 4.5, 4.7, and 4.85 V versus Li^+/Li during charge and 4.6, 4.4, 4.2, and 4.1 V versus Li^+/Li on discharge. The Raman spectra (see figure 3(b)) from *in situ* measurements were performed on cells subjected to galvanostatic charge and discharge to various potentials: 4.5, 4.7, 4.85, and 5.0 V during charging, and 4.6, 4.4, 4.2, 4.0 and 3.0 V during discharging. In the spectrum of the pristine graphite, two first-order scattering bands were observed at 1575 cm^{-1} and 1348 cm^{-1} attributed to the G and D band, along with the second-order scattering (2D) bands at 2678 and 2711 cm^{-1}. The presence of the D band (also known as the defect band) usually indicates that the material has structural defects related to stacking faults, point defects, and crystallite edges [42, 48]. The G band originates from the in-plane vibrations of the sp^2 carbon–carbon bonds with an E$_{2g2}$ symmetry [48, 49]. The intercalation of ions disrupts the stacking sequence of graphene layers, causing a shift in the G-band and the emergence of new bands [23]. Depending on the extent of intercalation, there will be periodic arrangements of occupied and unoccupied layers between the graphene planes, until all are filled with the anions. The staged GICs can be identified using their unique Raman spectra showing peaks at different wavenumbers and with variable intensities.

As can be seen in figure 3(b), during the intercalation process at 4.5 V, two more bands emerged at 1609 cm^{-1} and 1632 cm^{-1} in addition to the G band mode located at 1585 cm^{-1}. The first two bands at higher wavenumbers result from interactions between the bounding (b) graphene layers and the intercalated FSI anions. In contrast, the second one, situated at a lower wavenumber, originates from interior (i) graphene layers adjacent to other graphene layers. The former is designated as E$_{2g2}$(b) mode and the latter as the E$_{2g2}$(i) mode. Thus, the anion intercalation in graphite is generally indicated by the emergence of the E$_{2g2}$(b) peak, which signals the charge transfer process between FSI anions and the boundary graphene layers [16]. As more graphite layers were intercalated at 4.7 V, both bands underwent a blue shift, and the intensity of the E$_{2g2}$(i) band diminished as opposed to E$_{2g2}$(b) band, whose intensity dramatically increased. At 4.85 V, the E$_{2g2}$(i) mode disappeared, followed by an increase in the intensity of the E$_{2g2}$(b) mode, which further shifted to 1620 cm^{-1}. Interestingly, an additional band was observed at 1631 cm^{-1} as a shoulder on the E$_{2g2}$(b) mode, which indicated a phase transition of the GIC (possibly from stage-III to stage-II). When stage-II GIC has formed, each graphene layer will be bounded by a layer of anions on one side and a graphene layer on the other side, i.e., adjacent layers of graphene and intercalated anions. This transition could be seen as the highest peak in the differential capacity plot in figure 3(a). Upon further intercalation at 5.0 V, the E$_{2g2}$(b), previously observed at 1620 cm^{-1}, was no longer detected, and a single, intense peak was observed at 1635 cm^{-1}, indicating that the stage transition was complete, and a GIC with few or no interior layers was formed (stage-II phase) [27, 42, 47]. The reverse trend was observed during the deintercalation process. After discharge to 4.6 V, a new band (E$_{2g2}$(i)) located at 1622 cm^{-1} emerged next to the E$_{2g2}$(b) band at 1633 cm^{-1}. The new band indicated the extraction of FSI anions from the graphite, leading to the re-emergence of interior graphene layers within the structure. As the graphite was further discharged, the E$_{2g2}$(i) intensity increased continuously while the E$_{2g2}$(b) intensity decreased, and both peaks shifted to lower wavenumbers. Finally, after discharging to 3 V, the G band grew more intense and moved to
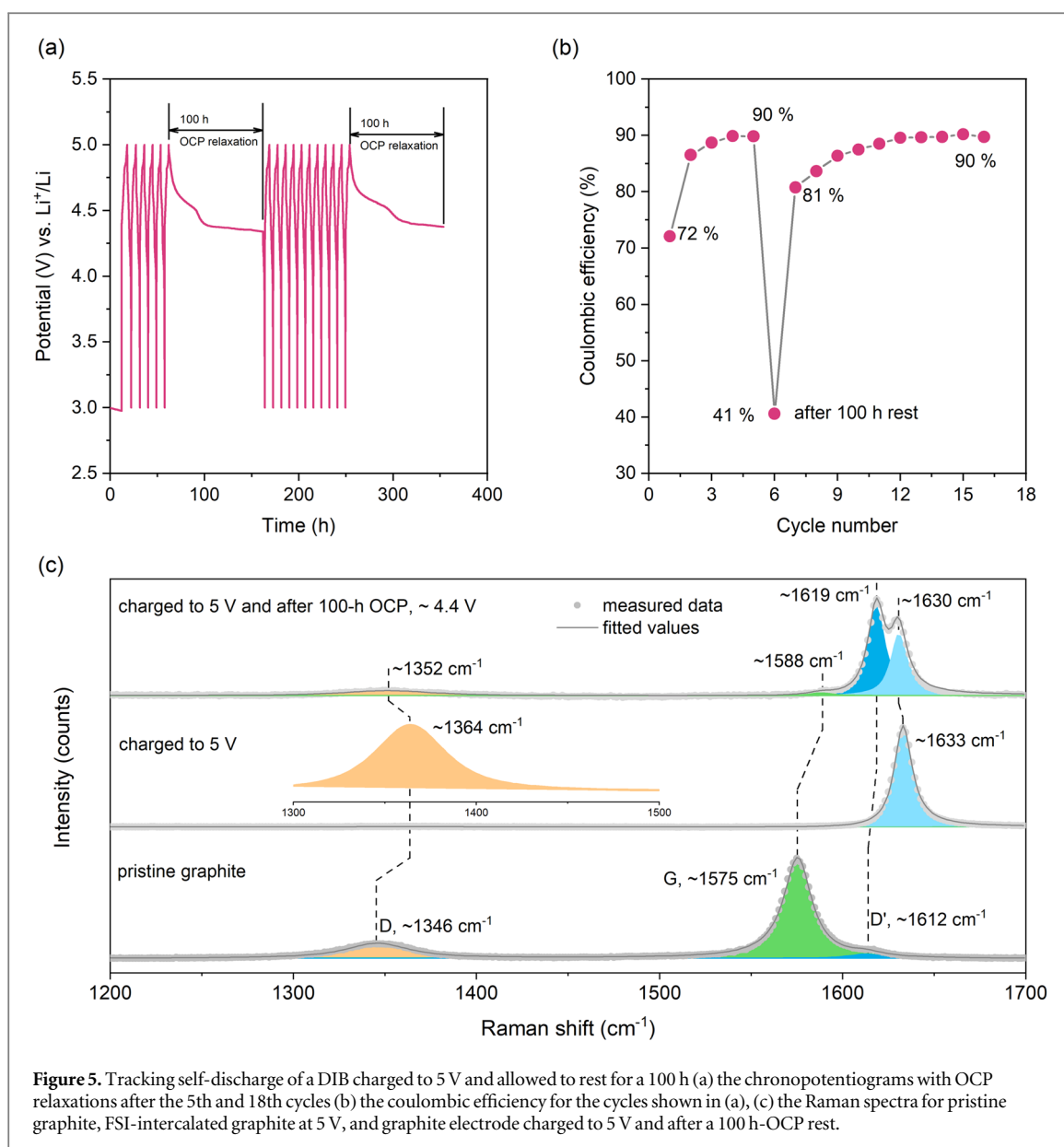
Figure 4. Raman spectra measured *ex situ* on graphite electrodes during charge and discharge processes after self-discharge relaxations at OCP over (a) <10 h, and (b) ~1 week.

approximately the starting frequency of ~1585 cm^{-1}. However, the E$_{2g2}$(b) band did not disappear entirely but instead manifested as a shoulder on the most intense G band (corresponding to E$_{2g2}$(i)). That means some FSI anions remained trapped in the graphite structure.

Having identified structural changes at the potentials of interest, we further investigated how self-discharge, caused by parasitic reactions, affected the structure of FSI-intercalated graphite electrodes. The graphite electrodes were charged and discharged to the potentials indicated in figure 3(a) and stored in the cells for short (<10 h) and long (1 week) durations before ex situ Raman spectroscopy measurements (figure 4). Similar to the *in situ* measurements, the Raman spectrum for the GIC obtained at 4.5 V was marked with the G band splitting into two bands for the reasons explained previously. Still, the shifts and the relative intensities varied depending on how long the electrodes rested in contact with the electrolyte inside the cells. The Raman shifts observed in figure 4 were generally similar to the spectra from *in situ* measurements. However, more pronounced differences were witnessed as charging proceeded to higher potentials. In all cases, the two bands at 4.7 V shifted to higher wavenumbers, and the intensity of the E$_{2g2}$(i) bands (1586–1588 cm^{-1}) decreased, while the E$_{2g2}$(b) band (1612–1618 cm^{-1}) generally intensified.

Interestingly, the duration of OCP relaxation caused a significant change in the spectrum for the GICs prepared at 5 V. The E$_{2g2}$(i) band was barely visible in the ex situ spectrum after short OCP relaxation (figure 4(a)) but was significantly intense in the graphite electrode from the cell that rested for about 1 week at OCP (figure 4(b)). The E$_{2g2}$(b), observed at 1635 cm^{-1} in the *in situ* spectrum, shifted to 1617 cm^{-1} after self-discharge over 1 week. At the end of the deintercalation the E$_{2g2}$(i) (~1580 cm^{-1}) band did not return to the original position (~1575 cm^{-1}), which evidently showed that some anions still remained in the graphite structure. Overall, these measurements strongly indicated that considerable amount of FSI anions was lost from the graphite structure due to the self-discharge process.

The potential evolution during OCP relaxation of a fully-charged DIB was used to further assess the long-term stability of fully FSI-intercalated graphite electrodes. The test was followed by ex situ Raman spectroscopy. As shown in figure 5(a), the cell was initially cycled five times between 3 and 5 V at 20 mA g^{-1}. At the 6th cycle, the cell was fully charged to 5.0 V and then allowed to relax at OCP for about 100 h. It was observed that the potential declined gradually to ~ 4.5 V over 30 h, after which it decreased more sharply to ~ 4.4 V. Finally, the cell attained a relatively stable potential at ~ 4.34 V at 100 h. When the cell discharged, the coulombic efficiency was only ~ 40% as opposed to ~ 90% observed for the previous cycle (figure 5(b)). The coulombic efficiency increased from 80% on the 7th to ~ 90% on the 16th cycle. Afterwards, the cell was fully charged to 5 V and allowed to rest at OCP for 100 h, at which the potential was 4.38 V. The graphite electrode was then removed from the cell in a glove box, and a Raman spectrum was collected (see figure 5(c)). Before self-discharge, as discussed above, in the spectrum for the GIC at 5.0 V, the E$_{2g2}$(i) peak, was located at about 1633 cm^{-1}. After self-discharge over 100 h, three overlapping bands were observed. The overlap of the E$_{2g2}$(i) with E$_{2g2}$(b) modes pointed to the release of the intercalated FSI anions from the graphite host, which caused the band at 1633 cm^{-1} to shift to 1630 cm^{-1}. Additional bands could be seen around 1619 cm^{-1} and 1588 cm^{-1} as other GIC phases formed. These findings and the rate characteristics indicated that the concentrated electrolyte used in this study did not entirely eliminate parasitic reactions at the CEI. As a result, only the low-stage GICs (typically stage-IV) are sufficiently stable. It should be noted that the Raman measurements on anion-intercalated GICs must be performed without too much exposure to the electrolyte, preferably *in situ*, in order to accurately capture the structural subtility.

Figure 5. Tracking self-discharge of a DIB charged to 5 V and allowed to rest for a 100 h (a) the chronopotentiograms with OCP relaxations after the 5th and 18th cycles (b) the coulombic efficiency for the cycles shown in (a), (c) the Raman spectra for pristine graphite, FSI-intercalated graphite at 5 V, and graphite electrode charged to 5 V and after a 100 h-OCP rest.

Apart from Raman spectroscopy, the stability of FSI-intercalated graphite electrodes was assessed using *operando* gas pressure measurements on three-electrode cells consisting of LTO and graphite electrodes with a separate Li reference (see a schematic of the cell in figure S3(a)). As shown in figures S3(b)–(d), extended voltage plateaus emerged in the galvanostatic curves when the cell potential reached 4.95 V versus Li^+/Li. The phenomenon was accompanied by a drastic pressure increase inside the cell, indicative of the generation of gaseous products accompanying the FSI intercalation reactions. The overall gas pressures slightly decreased when charging was limited to lower cut-off potentials of 4.9 V and 4.84 V. The total pressure reached a plateau at open-circuit potential relaxation at the end of the deintercalation process at 3 V, i.e., at the end of the redox reaction. The trend confirmed that the pressure buildup resulted from electrochemical processes that entailed the oxidative decomposition of the electrolyte and possibly surface oxidation of the graphite in the presence of traces of water [50], resulting in gases such as CO, CO_2, H_2 and SO_2 [36, 37, 51]. As reported in previous publications, some gases could also be generated on the LTO electrode [52]. Further research is needed to identify the nature and origin these gases using advanced techniques like online electrochemical mass spectrometry.

4. Conclusions

This study investigated intercalation behaviour and self-discharge of FSI-intercalated graphite compounds in DIBs using an EMC-based electrolyte containing 4 M LiFSI salt. Raman spectroscopy, performed both ex situ and *in situ*, revealed the intricate structural changes accompanying the formation of various FSI-intercalated

graphite compounds. Initially, the characteristic bands of pure graphite were observed at $\sim$1347 cm^{-1} (D band) and $\sim$1575 cm^{-1} (G band). Additional bands emerged at higher frequencies in the course of FSI intercalation. When charged to 4.9 to 5 V, a new, intense band appeared at $\sim$ 1632–1635 cm^{-1}, attributed the formation of the blue-coloured stage-II GIC. On discharge, FSI extraction caused a series of phase transformations in the different stage-GICs, as verified by the bands in the Raman spectra. After discharge to 3 V, mainly the D, G, and 2D bands were observed at frequencies close to that of pristine graphite, thereby confirming the chemical reversibility of FSI intercalation in the electrolyte under consideration. The impact of self-discharge upon OCP relaxation was tracked using Raman spectroscopy and operando gas pressure measurements. During OCP relaxation, the potential declined gradually to $\sim$ 4.5 V over 30 h, decreasing to a practically stable potential of $\sim$ 4.34 V over 100 h. A considerably reduced coulombic efficiency ($\sim$ 40%) was observed for the DIB after the OCP rest, though it increased to about 90% in the subsequent cycles. Compared to the spectrum measured at 5.0 V, which showed a single, intense band at 1633 to 1635 cm^{-1}, self-discharge caused the emergence of three bands at 1630 cm^{-1}, 1619 cm^{-1}, and 1588 cm^{-1}. Such changes in the spectrum indicated that FSI anions were lost as the cell rested at OCP for 100 h. The observation implied that the FSI-intercalated GICs (with low-stage index) were only kinetically stable in contact with the electrolytes. Furthermore, increasing the upper cut-off potential intensified the release of gaseous products generated in the cell, as indicated by operando gas pressure measurements. Similar studies will be needed to clearly show the impact of salt and solvent additives on the eventual stability of anion-intercalated graphite electrodes and their performance in DIBs.

Acknowledgments

Data availability statement

We have not yet decided which data repository/host to use. The data cannot be made publicly available upon publication because the cost of preparing, depositing and hosting the data would be prohibitive within the terms of this research project. The data that support the findings of this study are available upon reasonable request from the authors.

Conflict of interest

The authors declare no competing interests.

ORCID iDs

Habtom D Asfaw 🅾 https://orcid.org/0000-0001-5861-4281

References

[1] Enoki T, Suzuki M and Endo M 2003 *Graphite intercalation compounds and applications.* (Oxford University Press)
[2] Li Y *et al* 2019 Intercalation chemistry of graphite: alkali metal ions and beyond *Chem. Soc. Rev.* **48** 4655–87
[3] Dresselhaus M S and Dresselhaus G 1981 Intercalation compounds of graphite *Adv. Phys.* **30** 139–326
[4] Wei Y *et al* 2023 An ultrahigh-mass-loading integrated free-standing functional all-carbon positive electrode prepared using an architecture tailoring strategy for high-energy-density dual-ion batteries *Adv. Mater.* **35** 2302086
[5] Yang Z *et al* 2011 Electrochemical energy storage for green grid *Chem. Rev.* **111** 3577–613
[6] Wu S, Zhang F and Tang Y 2018 A novel calcium-ion battery based on dual-carbon configuration with high working voltage and long cycling life *Adv. Sci.* **5** 1701082
[7] Asfaw H D and Kotronia A 2022 A polymeric cathode-electrolyte interface enhances the performance of MoS2-graphite potassium dual-ion intercalation battery *Cell Reports Physical Science.* **3** 100693
[8] Kravchyk K V and Kovalenko M V 2019 Rechargeable dual-ion batteries with graphite as a cathode: key challenges and opportunities *Adv. Energy Mater.* **9** 1901749
[9] Kravchyk K V *et al* 2018 High-energy-density dual-ion battery for stationary storage of electricity using concentrated potassium fluorosulfonylimide *Nat. Commun.* **9** 4469
[10] Kravchyk K V, Seno C and Kovalenko M V 2020 Limitations of chloroaluminate ionic liquid anolytes for aluminum–graphite dual-ion batteries *ACS Energy Lett.* **5** 545–9
[11] Kravchyk K V and Kovalenko M V 2020 Aluminum electrolytes for Al dual-ion batteries *Commun. Chem.* **3** 120
[12] Kravchyk K V *et al* 2017 Efficient aluminum chloride–natural graphite battery *Chem. Mater.* **29** 4484–92
[13] Placke T *et al* 2018 Perspective on performance, cost, and technical challenges for practical dual-ion batteries *Joule.* **2** 2528–50
[14] Zhang X *et al* 2016 A novel aluminum–graphite dual-ion battery *Adv. Energy Mater.* **6** 1502588

[15] Wang M 2018 Reversible calcium alloying enables a practical room-temperature rechargeable calcium-ion battery with a high discharge voltage *Nat. Chem.* **10** 667–72

[16] Kotronia A *et al* 2021 Nature of the cathode–electrolyte interface in highly concentrated electrolytes used in graphite dual-ion batteries *ACS Appl. Mater. Interfaces* **13** 3867–80

[17] Kotronia A *et al* 2023 Impact of binders on self-discharge in graphite dual-ion batteries *Electrochem. Commun.* **146** 107424

[18] Münster P *et al* 2019 Enabling high performance potassium-based dual-graphite battery cells by highly concentrated electrolytes *Batteries & Supercaps* **2** 992–1006

[19] Kotronia A, Asfaw H D and Edström K 2023 Evaluating electrolyte additives in dual-ion batteries: overcoming common pitfalls *Electrochim. Acta* **459** 142517

[20] Read J A *et al* 2014 Dual-graphite chemistry enabled by a high voltage electrolyte *Energy Environ. Sci.* **7** 617–20

[21] Wang Y *et al* 2022 An all-fluorinated electrolyte toward high voltage and long cycle performance dual-ion batteries *Adv. Energy Mater.* **12** 2103360

[22] Beltrop K *et al* 2018 Enabling bis(fluorosulfonyl)imide-based ionic liquid electrolytes for application in dual-ion batteries *J. Power Sources* **373** 193–202

[23] Han C *et al* 2023 Solvation structure modulation of high-voltage electrolyte for high-performance k-based dual-graphite battery *Adv. Mater.* **35** 2300917

[24] Sui Y *et al* 2020 Dual-ion batteries: the emerging alternative rechargeable batteries *Energy Storage Mater.* **25** 1–32

[25] Jiang X *et al* 2019 Electrolytes for dual-carbon batteries *Chem. Electro. Chem.* **6** 2615–29

[26] Miyoshi S *et al* 2016 Dual-carbon battery using high concentration lipf6in dimethyl carbonate (DMC) electrolyte. *J. Electrochem. Soc.* **163** A1206–13

[27] Seel J A and Dahn J R 2000 Electrochemical intercalation of PF[sub 6] into graphite *J. Electrochem. Soc.* **147** 892

[28] Gao J *et al* 2015 Intercalation manners of perchlorate anion into graphite electrode from organic solutions *Electrochim. Acta* **176** 22–7

[29] Xu K 2004 Nonaqueous liquid electrolytes for lithium-based rechargeable batteries *Chem. Rev.* **104** 4303–418

[30] Kotronia A *et al* 2021 Ternary ionogel electrolytes enable quasi-solid-state potassium dual-ion intercalation batteries *Advanced Energy and Sustainability Research.* **3** 2100122

[31] Tan H *et al* 2021 Synergistic PF6− and FSI− intercalation enables stable graphite cathode for potassium-based dual ion battery *Carbon* **178** 363–70

[32] Fang C *et al* 2021 Large-molecule decomposition products of electrolytes and additives revealed by on-electrode chromatography and MALDI *Joule* **5** 415–28

[33] Sahore R, Dogan F and Bloom I D 2019 Identification of electrolyte-soluble organic cross-talk species in a lithium-ion battery via a two-compartment cell *Chem. Mater.* **31** 2884–91

[34] Henschel J *et al* 2020 Clarification of decomposition pathways in a state-of-the-art lithium ion battery electrolyte through 13C-labeling of electrolyte components *Angew. Chem. Int. Ed.* **59** 6128–37

[35] Rowden B and Garcia-Araez N 2020 A review of gas evolution in lithium ion batteries *Energy Reports* **6** 10–8

[36] Jusys Z *et al* 2019 A novel DEMS approach for studying gas evolution at battery-type electrode|electrolyte interfaces: high-voltage LiNi0.5Mn1.5O4 cathode in ethylene and dimethyl carbonate electrolytes *Electrochim. Acta* **314** 188–201

[37] Tong X *et al* 2021 High oxidation potential ≈6.0 V of concentrated electrolyte toward high-performance dual-Ion battery. *Adv. Energy Mater.* **11** 2100151

[38] Nozu R *et al* 2020 Tetraethylammonium tetrafluoroborate additives for suppressed gas formation and increased cycle stability of dual-ion battery *Electrochim. Acta* **337** 135711

[39] Yu Z *et al* 2019 Flexible stable solid-state Al-Ion batteries *Adv. Funct. Mater.* **29** 1806799

[40] Huang Z *et al* 2021 Manipulating anion intercalation enables a high-voltage aqueous dual ion battery *Nat. Commun.* **12** 3106

[41] Rothermel S *et al* 2014 Dual-graphite cells based on the reversible intercalation of bis(trifluoromethanesulfonyl)imide anions from an ionic liquid electrolyte *Energy Environ. Sci.* **7** 3412–23

[42] Balabajew M *et al* 2016 *In-situ* raman study of the intercalation of bis(trifluoromethylsulfonyl)imid ions into graphite inside a dual-ion cell *Electrochim. Acta* **211** 679–88

[43] Elia G A *et al* 2020 Simultaneous x-ray diffraction and tomography operando investigation of aluminum/graphite batteries *Adv. Funct. Mater.* **30** 2003913

[44] Pan C-J *et al* 2018 An operando x-ray diffraction study of chloroaluminate anion-graphite intercalation in aluminum batteries *Proc. Natl. Acad. Sci.* **115** 5670

[45] Losq C L 2018 Rampy: a Python library for processing spectroscopic (IR, Raman, XAS.) data. (0.4.6) (https://doi.org/10.5281/zenodo.4715040)

[46] Brown S D M *et al* 2001 Origin of the breit-wigner-fano lineshape of the tangential g-band feature of metallic carbon nanotubes *Phys. Rev. B* **63** 155414

[47] Read J A 2015 *In-situ* studies on the electrochemical intercalation of hexafluorophosphate anion in graphite with selective cointercalation of solvent *The Journal of Physical Chemistry* C **119** 8438–46

[48] Tuinstra F and Koenig J L 1970 Raman spectrum of graphite *J. Chem. Phys.* **53** 1126–30

[49] Ferrari A C 2007 Raman spectroscopy of graphene and graphite: disorder, electron–phonon coupling, doping and nonadiabatic effects *Solid State Commun.* **143** 47–57

[50] Rinkel B L D *et al* 2020 Electrolyte oxidation pathways in lithium-ion batteries *JACS* **142** 15058–74

[51] Sångeland C *et al* 2021 Decomposition of carbonate-based electrolytes: differences and peculiarities for liquids vs. polymers observed using operando gas analysis *Batteries & Supercaps* **4** 785–90

[52] He Y-B *et al* 2012 Gassing in Li4Ti5O12-based batteries and its remedy *Sci. Rep.* **2** 913